The metallophilic interaction between cyclometalated complexes: photobiological applications
Zhou, X.

Citation
Zhou, X. (2021, May 26). *The metallophilic interaction between cyclometalated complexes: photobiological applications*. Retrieved from https://hdl.handle.net/1887/3158746

Cover Page

Universiteit Leiden

Author: Zhou, X.
Title: The metallophilic interaction between cyclometalated complexes: photobiological applications
Issue Date: 2021-04-08

4

Intracellular dynamic assembly of deep-red emitting supramolecular nanostructures based on Pt…Pt metallophilic interaction

Many nanoparticle drug delivery systems end up in the endosome or lysosome because they are made of covalent or kinetically trapped self-assembled systems (e.g. liposomes) that cannot escape the membrane of the endo-lysosomal intracellular vesicles after endocytic uptake. To be able to reach other organelles, nanoparticles would hence need to either be made from a kinetically labile interaction that allows re-assembly of the nanoparticles inside the cell following uptake, or, to be taken up by a mechanism that short-circuits the classical endocytosis pathway. In this work, we studied the intracellular fate of nanorods generated by self-assembly via the Pt…Pt metallophilic interaction of cyclometalated platinum(II) compounds. Outside cells, these deep-red emissive nanostructures (638 nm excitation, ~ 700 nm emission) are stabilized by proteins in cell medium. Once in contact with A549 lung cancer cells, they cross the cell membrane via dynamin- and clathrin-dependent endocytosis. However, time-dependent confocal colocalization and cellular electron microscopy demonstrated that they directly move to the mitochondria without passing by the lysosomes. Altogether, this study suggests that the Pt…Pt interaction is strong enough to generate emissive, aggregated nanoparticles inside the cell, but labile enough to allow these nanostructures to reach the mitochondria without being trapped, or passing by, the lysosomes. These findings open a new venue for the development of supramolecular theranostic nanoplatforms based on the Pt…Pt interaction.

4.1 Introduction

The metallophilic M…M interaction, which is based on d orbital overlap, has been described for planar d^8 and d^{10} metals, such as gold(I), nickel(II), palladium(II) and platinum(II) complexes.[1-4] It affords fascinating supramolecular aggregated systems with unique optical or properties such as "organic" light-emitting diodes or biosensors.[5-12] The emissive properties arising when the Pt...Pt interaction takes place are attributed to low-energy metal-metal-to-ligand charge-transfer (MMLCT) or ligand-to-metal-metal charge-transfer (LMMCT) transitions, which also generate good absorbance in the visible region of the spectrum.[11, 13] These bands are attributed to the low HOMO-LUMO gap arising when platinum(II) centers come close enough for their d_z^2 orbitals to interact; this interaction is typically facilitated by π-π stacking of the ligands bound to platinum, which counter-balance the electrostatic repulsion exerted by the positively charged metal centers.[14] Overall, red light absorbance and deep-red luminescence are both particularly important for intracellular imaging and phototherapeutic compounds, where light penetration of tissues is critical.[15, 16]

Independently from their ability to engage in metallophilic interaction, phosphorescent platinum complexes show several advantages for live-cell imaging, compared with organic dyes, such as large Stokes shift, reduced photobleaching, and long excited state lifetimes.[6, 17-21] In parallel, the clinical success of cisplatin has stimulated research towards new platinum-based anticancer drugs and bioinorganic applications of platinum-organic compounds.[22-24] Many reports focus on pincer-like platinum complexes based on tridentate polypyridyl ligands because of their tunable photophysical properties, the existence of various mechanisms inducing cytotoxicity, and supramolecular assembly derived from the Pt...Pt metallophilic interaction.[14, 24-28] Che *et al.* reported a series of complexes generating supramolecular polymers based on the Pt...Pt interaction can show pH-dependent emission in the lysosome of cells.[18] Meanwhile, the role of proteins in the self-assembly of Pt compounds is very diverse; for example, Cola *et al.* reported that cell medium prevented some platinum complexes to be internalized by the cells.[17] Overall, little is known about the morphology of supramolecular polymers based on the Pt…Pt interaction in cell medium or inside cells, their mechanism of cellular uptake, and the dynamics of their intracellular distribution.

These questions have become particularly relevant because of the emergence of nanomaterials as functional delivery platforms for the imaging and therapy of cancer.[29-31] Many types of organic and inorganic theranostic nanosystems have been developed, derived from *e.g.* lipid-based nanoparticles, polymers, lanthanide fluorides, or silica nanoparticles.[31-35] Endocytosis is

considered to be the major cellular uptake mechanism for nanoparticles, as a consequence of which they typically end up in the endosome or lysosome.[36] The lysosome, in particular, is responsible for the digestion of extracellular substances, and it generates for this aim abundant hydrolytic enzymes and an acidic environment, which limits many nano-drug delivery systems by preventing drug release into the cytosol.[37, 38] Thus, nanoparticles capable of endo-lysosomal escape or avoiding lysosomes are of great interest. In this work, we were able to generate self-assembled nanoparticles based on the Pt...Pt interaction that can move from the cell membrane to mitochondria directly with exceptional uptake efficiency, without the assistance of lysosome. These nanoparticles are built from a molecularly well-defined cyclometalated platinum complex, which makes these nanomaterials particularly easy to prepare in a reproducible manner. Because of the aggregation-induced red absorption and deep-red emission of these nanostructures, their low photobleaching, and the high electron density generated by the platinum centers, it is possible to monitor in cells their morphology, fate, and dynamic reorganization by a combination of confocal microscopy, cell electron microscopy, and flow cytometry, effectively demonstrating cellular uptake by endocytosis, endosomal escape, and relocation into the mitochondria.

4.2 Results

4.2.1 Synthesis and characterization of two cyclometalated platinum(II) complexes. Two isomeric complexes **[PtMeL^1]OAc** (**[1]OAc**) and **[PtMeL^2]OAc** (**[2]OAc**, Figure 4.1) were prepared by cyclometalation of the known tetradentate ligands **HMeL^1** and **HMeL^2**,[39] using platinum(II) acetylacetonate in boiling acetic acid. The compounds **[1]$^+$** and **[2]$^+$** differ by the position of the platinum-carbon bond: in **[1]$^+$** it is closer to the bridging NMe group than in **[2]$^+$**. The ^{1}H NMR spectra obtained for each complex were different at low (2 mg/mL MeOD) vs. high (7 mg/mL MeOD) concentration (Figure AIII.1), which suggested some form of supramolecular assembly in this solvent. The crystal structure of **[2]PF$_6$** confirmed this tendency: The crystal packing of **[2]PF$_6$** (Figure 4.1b) clearly identified one short (3.3216(5) Å) and one long (4.2572(6) Å) intermolecular Pt…Pt distance. The short Pt…Pt distance also corresponded to short distances between the aromatic rings of the parallel cyclometalated ligand (the shortest distance around 3.5 Å), demonstrating strong π-π stacking as well. Altogether the crystal suggested the formation of supramolecular dimers in the solid state.
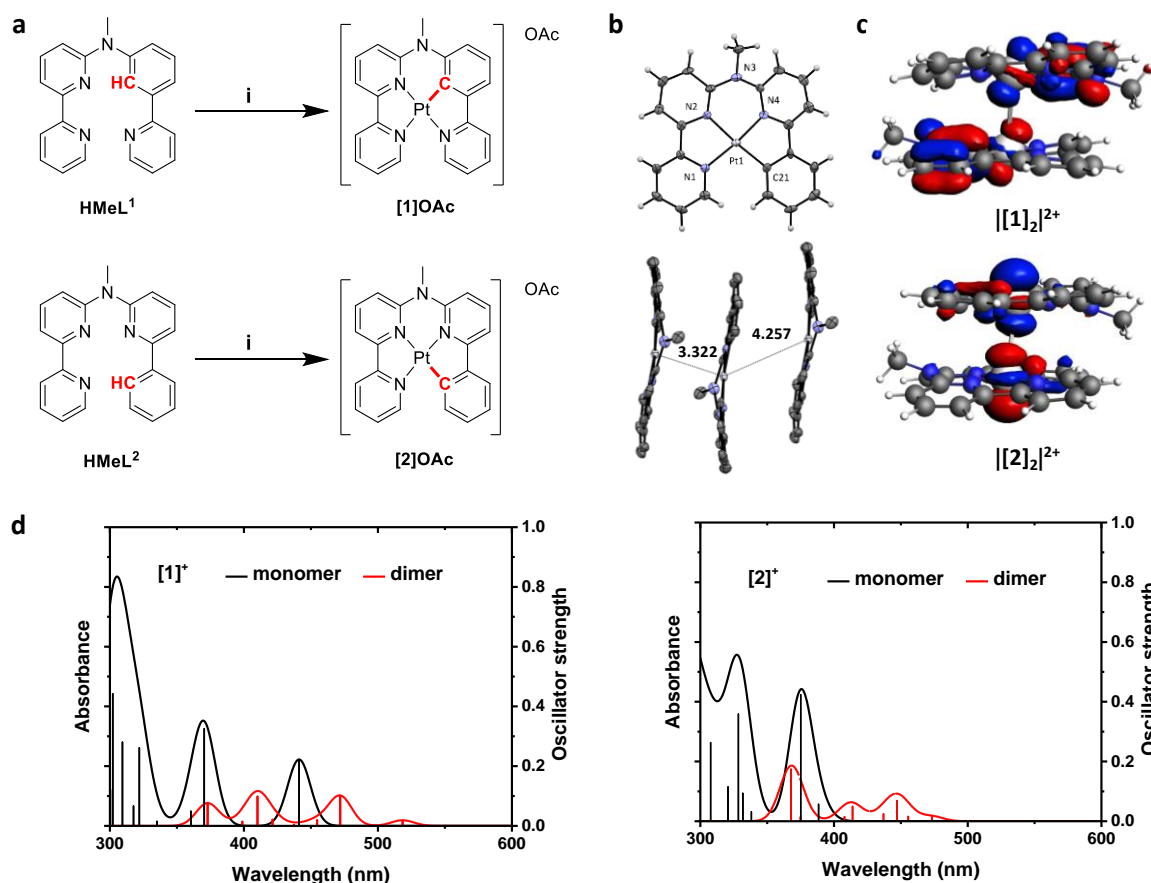
Figure 4.1 *(a) Synthesis of **[1]OAc** and **[2]OAc**. Reaction condition: i) Platinum(II) acetylacetonate (1 eq.), tetrabutylammonium acetate, CH₃COOH, N₂, 135 °C, 6 days; 32% yield for **[1]OAc** and 93% yield for **[2]OAc**. (b) Displacement ellipsoid plot (50% probability level) and packing of **[2]PF₆** at 110(2K). Element color code: gray = C, blue = N, white = Pt and H; anion has been omitted for clarity; Pt...Pt distances are given in Å. (c) HOMO of |[1]₂|²⁺ and |[2]₂|²⁺ showing the d_z² overlap, calculated by DFT at the PBE0/TZP/COSMO level in water. Element color code: gray = C, blue = N, white = Pt and H. (d) Excitation spectra of **[1]⁺** and **[2]⁺** in the monomeric and dimeric states according to TDDFT calculations.*

According to density functional theory (DFT) and time-dependent density functional theory calculations (TDDFT) run at the PBE0/TZP/COSMO level for both monomolecular complexes in water, the calculated HOMO-LUMO transition of **[1]⁺** is at much lower energy (441 nm) than that of **[2]⁺** (375 nm, Table AIII.1). As the HOMO is based on the lone pair of the NMe bridge, and the LUMO is essentially located on the bipyridine part of the ligand, the HOMO in **[1]⁺** is more destabilized by the closer, electron-rich cyclometalated bond, than the HOMO in **[2]⁺**, while both bpy-based LUMOs are essentially at the same energy level. The dimers of complexes were also modeled by DFT. According to these calculations, dimers form despite

the electrostatic repulsion exerted by the monocationic complexes. Their HOMO is composed of the two d_z2 orbitals on the platinum centers interacting in an antibonding fashion, with an additional contribution from π orbitals of the ligands (Figure 4.1c). The calculated Pt…Pt distance was short (3.34 Å for **[1]**[+] and 3.26 Å for **[2]**[+]), confirming that in such dimers the metallophilic interaction is strong, and occurs as a result of a combination of d_{z2} axial overlap and π-π stacking. Besides, the HOMO-LUMO energy gaps of both complexes significantly decreased in the dimer state compared with the monomer (Figure AIII.2), especially for **[2]**[+], from 4.13 eV (monomer) to 3.39 eV (dimer). Further TDDFT calculation demonstrated that the dimer of both complexes shows a lower-energy absorbance band than their monomer, which can be attributed to a transition from the σ* orbital on the Pt…Pt axis to π* ligand-based orbitals, corresponding to an MMLCT excited state. These results indicated that the aggregates of these complexes might be excited at a longer wavelength than the monomers.

4.2.2 Photophysical properties of platinum(II) complexes in the monomeric and aggregated states. The absorbance and normalized emission spectra of **[1]OAc** and **[2]OAc** (50 μM) in methanol, water, and Opti-MEM complete cell medium (2.5% V/V fetal calf serum (FCS)), are shown in Figure 4.2. The distinct absorbance of both isomers around 450 nm in MeOH solution can be attributed to their different HOMO-LUMO gap (Figure AIII.2), which critically depends on the proximity between the Pt-C bond and the non-bonding electron pair on the NMe bridge.[40] At low concentration in methanol (50 μM), both complexes showed a weak phosphorescence around 600 nm, characterized by low quantum yields (below 0.001, Table 4.1). The emission peaks at 588 nm (**[1]OAc**) and 616 nm (**[2]OAc**) in methanolic solution, which according to TDDFT can be assigned to ligand-to-ligand charge-transfer (LLCT) transitions with a small triplet metal-to-ligand charge-transfer ([3]MLCT) character. They also showed, in the same conditions, moderate quantum yields in generating singlet oxygen (ϕ_Δ = 0.44 for **[1]OAc**, 0.11 for **[2]OAc**), suggesting sub-optimal photodynamic properties in this solvent.

Spectroscopic measurements were then carried out in Milli-Q water (50 μM) to determine whether Pt...Pt interaction might occur in aqueous solution. In such conditions, moderate bathochromic shifts of the absorbance spectra of both compounds were found, which are typical indications for the formation of low-energy [3]MMLCT states derived from the Pt...Pt interaction (Figure 4.2a).[5, 6] This bathochromic shift of the absorbance was strongly enhanced when either compound (50 μM) was dissolved in Opti-MEM complete, and for **[2]OAc** a new absorption maximum appeared at 540 nm. The emission of both compounds was also red-shifted in pure

water with maxima at 655 and 691 nm for **[1]OAc**, 651 and 687 nm for **[2]OAc**, which are attributed to mixed ^{3}MLCT and ^{3}MMLCT transitions emission, probably from a mixture of monomers, oligomers, and polymers. In Opti-MEM complete, only the deep-red emission was observed (705 nm for **[1]OAc,** 699 nm for **[2]OAc**), which is the clear spectroscopic signature from ^{3}MMLCT transitions.[6] The singlet oxygen quantum yields in aqueous solutions were measured using the $^1O_2$ chemical sensor 9,10-anthracenediyl-bis(methylene)dimalonic acid (ABMDMA).[39] The value found for **[1]OAc** was lower (0.19) in the aggregated state in Opti-MEM complete medium, compared to the monomeric state in CD_3OD (0.44), while that of **[2]OAc** remained at a comparably low level (0.10) (Table 4.1, Figure AIII.3). The phosphorescence lifetime of both isomers in aerated MeOH, water, and Opti-MEM complete, showed biexponential decay (Figure AIII.4). The main component of the decay showed significant increase when changing the solvent from methanol to water to medium (Table 4.1). Meanwhile, the deep-red emission obtained in cell medium matched well, in terms of emission maximum, with the emission of the complexes in the solid state (Figure AIII.5). Interestingly, in the solid state, **[2]OAc** showed a much higher emission intensity than **[1]OAc**, which might be partially ascribed to the shorter Pt…Pt distance of **[2]OAc** and its comparatively stronger Pt…Pt interaction as demonstrated by DFT calculations (Pt…Pt distance: 3.34 Å for **[1]**$^+$ and 3.26 Å for **[2]**$^+$), and partially by different crystal structures. In conclusion, the red shifted absorbance and emission of both cyclometalated complexes in water and Opti-MEM solutions could be attributed to the formation of soluble nanoaggregates via Pt…Pt interaction, and it is similar to the spectroscopic signature of the solid state.

The strong deep-red emission of the platinum complexes as a solid or nanoparticle is attributed to the aggregation of the molecules via the Pt…Pt interaction, which represents a new mechanism for aggregation-induced emission (AIE) based on the metallophilic interaction. Up to now, the generally accepted mechanism of luminescence induction in AIE luminogens (AIEgens) is based on the restriction of intramolecular rotations and vibrations in supramolecular aggregates that, in the monomer, quench emission by vibronic coupling.[41-44] Rare cases of metal complexes that can generate luminescence in aggregated condition via metallophilic interaction, have lately attracted much interest.[23, 45-49] To demonstrate the aggregation-induced character of the Pt…Pt interaction, the emission spectrum was measured in methanol/diethylether mixtures containing 10-90 vol% ether. For both complexes upon the increase of the ether fraction from 10 to 60%, the emission gradually increased, indicating AIE was taking place (Figure 4.2b). However, above 60% of both complexes followed different

patterns. For **[2]OAc**, the luminescence at 700 nm increased suddenly at an ether fraction of 90%, which corresponds well with the strong red emission of the bulk solid state. For **[1]OAc**, the emission suddenly decreased and slightly red-shifted, which also indicated the formation of the bulk solid, which is a poorly emissive material (Figure AIII.5). This experiment confirmed the AIE property of these two complexes: the nanoaggregation taking place via Pt…Pt interaction leads to increased emission as long as the particles stay small enough to be solvated; upon precipitation at a high ether content, **[1]OAc** becomes poorly emissive while **[2]OAc** becomes more emissive, which corresponds to the bulk emission properties of the solids.
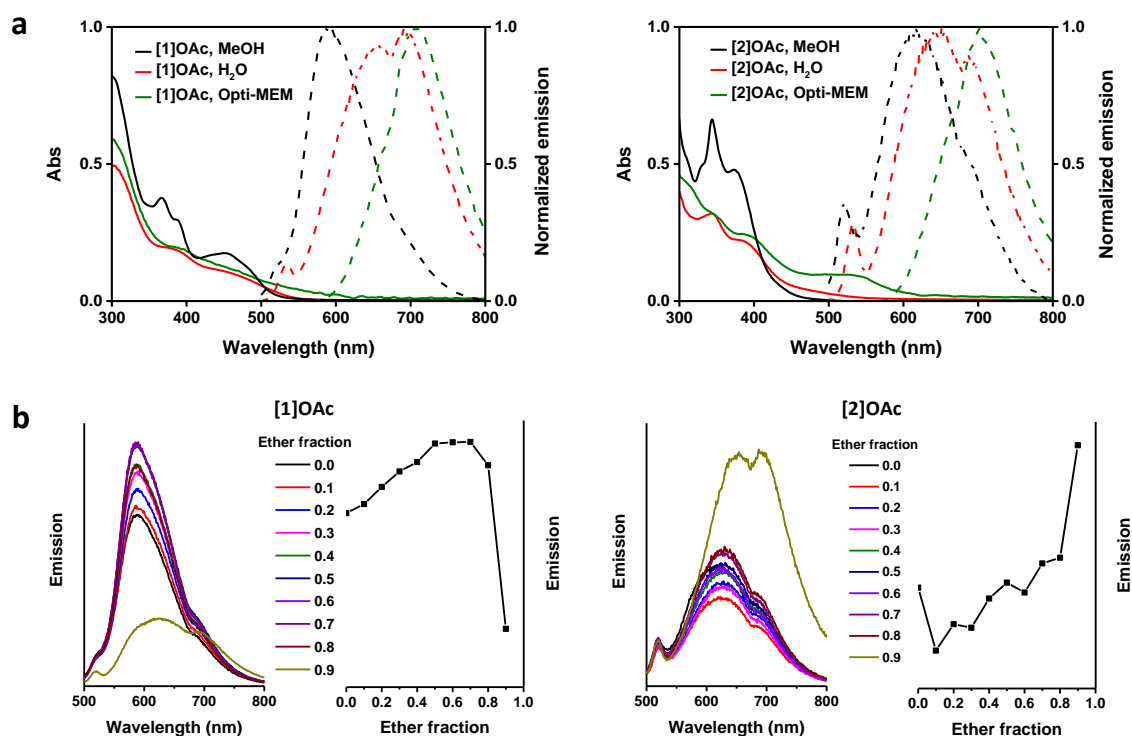

Figure 4.2 (a) The absorbance (solid lines) and emission spectra (dashed lines) of **[1]OAc** and **[2]OAc** in methanol (black), water (red) and Opti-MEM complete medium (green) (Concentration 50 µM, excitation 450 nm). (b) The emission spectra and emission intensity at 587 nm of **[1]OAc** (left) and **[2]OAc** (right) in methanol with different diethylether ratio (concentration 50 µM, excitation 450 nm).

Table 4.1 *Photophysical data for* ***[1]OAc*** *and* ***[2]OAc***.

complex		[1]OAc	[2]OAc
λ_{abs}, nm (ε x 10^3 M^{-1} cm^{-1})	H$_2$O	303 (8.9), 382 (3.4), 552 (0.25)	343 (6.1), 383 (4.2), 552 (0.22)
λ_{em}, nm[a]	MeOH	588	616
	H$_2$O	655, 691	651, 687
	Opti-MEM	705	699
	solid	727	721

$\phi_p{}^{b}$	MeOD		0.00125	0.00051
	H_2O		0.00080	0.00030
ϕ_Δ	MeOD[c]		0.44	0.11
	Opti-MEM[d]		0.19	0.10
Lifetime (ns) [e]	MeOH	τ_1	2.6±0.2 (19%)	0.61±0.05 (10%)
		τ_2	11±1 (81%)	5.7±0.5 (90%)
	H_2O	τ_1	0.5±0.2 (2%)	1.54±0.06 (13%)
		τ_2	23.7±0.5 (98%)	10.5±0.3 (87%)
	Opti-MEM	τ_1	3.96±0.07 (12%)	3.3±0.3 (9%)
		τ_2	29.6±0.3 (88%)	33.9±0.5 (91%)

[a] The emission spectra were measured in air condition. Excitation 450 nm, complex concentration 50 µM [b] Phosphorescence quantum yield measurements of **[1]OAc-[2]OAc** were carried out at 390 nm excitation wavelength in aerated water, or MeOD, using **[Ru(bpy)₃]Cl₂** (ϕ_p = 0.028 in water, 0.015 in MeOD) as standard. [c] Excitation wavelength 450 nm, air atmosphere. The absorption of each complex at 450 nm was adjusted to 0.1 to avoid the generation of excimer.[39] In CD_3OD by spectroscopic detection at 1270 nm; **[Ru(bpy)₃]Cl₂** was used as standard (ϕ_Δ = 73%). [d] In Opti-MEM complete using ABMDMA as $^{1}O_2$ probe; **[Ru(bpy)₃]Cl₂** was used as standard (φ_Δ = 14%).[39] [e] Excitation wavelength 375 nm.

4.2.3 Pt…Pt interaction induced supramolecular self-assembly. Interestingly, the aggregation-induced emission via Pt…Pt interaction does not only occur in methanol/ether mixtures, but also in several physiological solutions such as PBS and Opti-MEM medium. The size and number of nanoparticles obtained with platinum complexes **[1]OAc** and **[2]OAc** in water, PBS and Opti-MEM solution with different proteins (FCS, BSA and globulin) were investigated via dynamic light scattering (DLS) and transmission electron microscopy (TEM). In pure water, very few nanoparticles were detected (derived count rate (kcps)<700, Figure 4.3a); in PBS, the complexes showed significant aggregation (higher kcps values, kcps = 7627 and 1373 for **[1]OAc** and **[2]OAc** respectively, Figure 4.3a), indicating that the addition of salts might stimulate the self-assembly of the complexes. However, the time-evolution of the absorbance spectra of PBS solution of the complexes showed a gradual decrease (Figure AIII.6), suggesting slow precipitation (*i.e.* colloidal instability) in such conditions. When dissolved in the Opti-MEM medium with or without proteins, the size of the particles exhibited a large difference. This behavior resembles that of the palladium analogs of **[1]OAc** and **[2]OAc**, which form nanorods stabilized by FCS.[39] DLS measurements showed the presence of 100-500 nm nanoaggregates in Opti-MEM solutions containing FCS (v/v 2.5%, Opti-MEM complete), and of much larger aggregates (~1000 nm) indicative of precipitation in Opti-MEM medium deprived of proteins, suggesting that fetal calf serum plays a key role in the stabilization of the nanoaggregates in solution (Figure 4.3a, 4.3b, AIII.7). In the meantime, in Opti-MEM complete

solution the two platinum complexes showed a gradual increase in absorbance with time, which we attributed to increased light scattering due to the formation of nanoparticles; Reversely, the absorbance dramatically decreased when no FCS was present, which indicates fast precipitation (Figure AIII.6). When pure BSA (50 g/L) and globulin (30 g/L), the two main proteins in FCS, were dissolved in Opti-MEM medium and added to solutions of the complexes (50 µM), DLS indicated that both proteins play a key factor in the stabilization of the nanoparticles of these complexes (Figure 4.3a and AIII.7). TEM images (Figure AIII.8) showed that the aggregates in Opti-MEM complete were irregular round nanoparticles, with an average size of 56 nm for **[1]OAc** and 40 nm for **[2]OAc**, mixed with nanorod structures of 20 nm thickness. TEM also showed that **[2]OAc** resulted in more concentrated nanorod generation than **[1]OAc**, which might be attributed to the stronger Pt…Pt interaction. However, TEM is sub-optimal for determining the structures of self-assembled nanoparticles in solution, since structures are dried during preparation. To alleviate this problem, cryo-EM was carried out, which allows for observing the nanostructures in a vitrified solution state. The cryo-EM images of **[1]OAc** and **[2]OAc** (50 µM, Figure 4.3c) in Opti-MEM complete medium show clear nanorod structures with a width of around 30 nm, demonstrating the existence of supramolecular assembly via Pt…Pt interaction; specifically, no round particles were observed in cryo-EM images. The nanoparticles of **[1]OAc** were of smaller dimensions than that of **[2]OAc**, which matched with the TEM results. Cryo-EM imaging at higher magnifications for the nanoparticles of **[1]OAc** (Figure 4.3d), clearly revealed a crystalline structure for the nanorods, characterized by a high contrast hexagonal lattice captured in both x and z directions (repeating distance ~1.3 nm as indicated by fast Fourier transform). Overall, for both cyclometalated complexes, the Pt…Pt interaction observed in the solid state and solution by different spectroscopy techniques, triggered the self-assembly of platinum complexes into strongly deep-red emissive nanorod-like aggregates that are stabilized by serum proteins in cell medium.
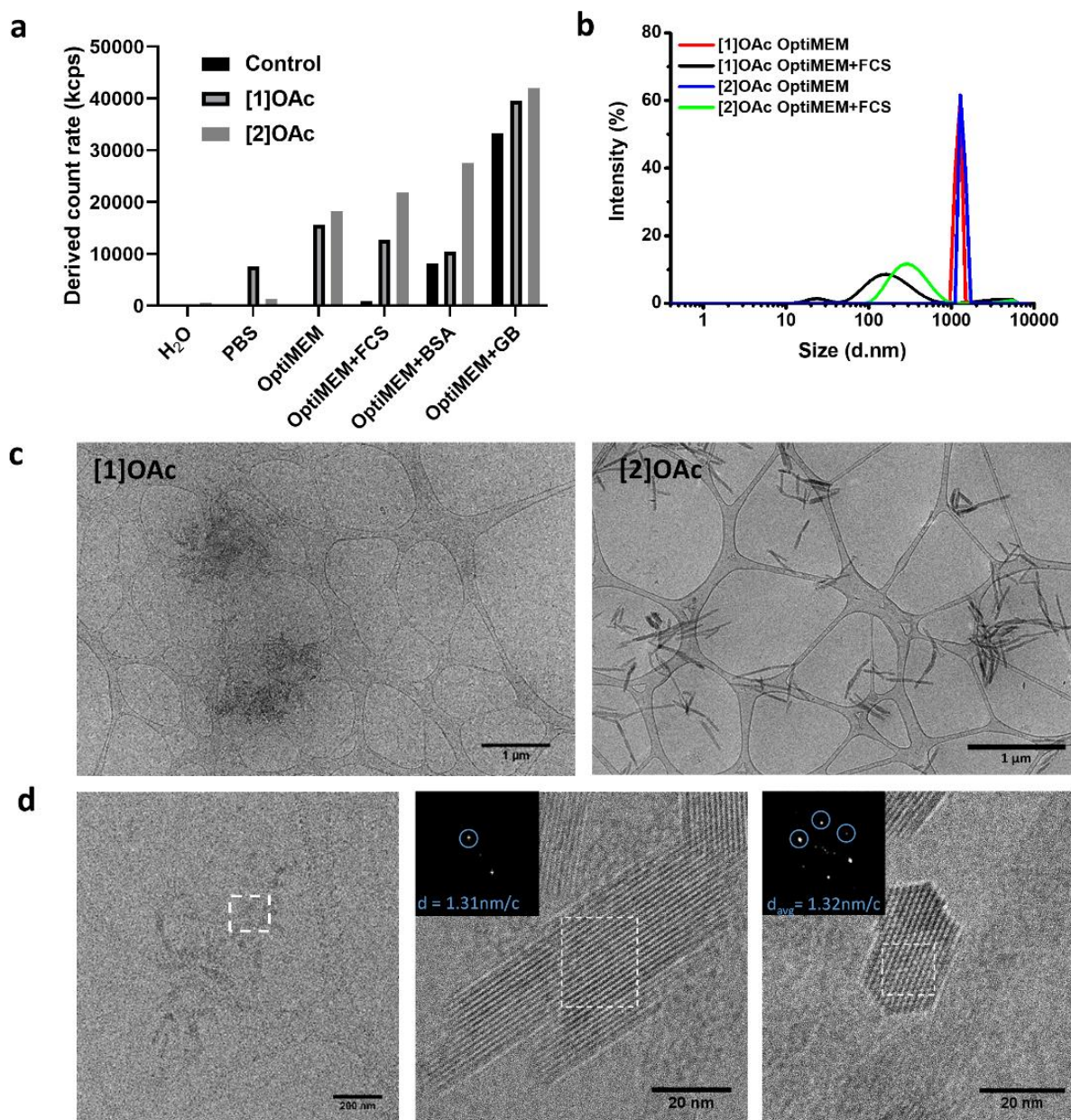
Figure 4.3 *(a) DLS mean count rate (kcps) of solutions of **[1]OAc** or **[2]OAc** in water (50 μM),*
PBS, Opti-MEM, Opti-MEM with fetal calf serum (FCS), serum albumin (BSA) and globulin
*(GB). (b) size distribution of complexes **[1]OAc** and **[2]OAc** (50 μM) in Opti-MEM medium*
with and without FCS (X-axis is the hydrodynamic diameter in nm, Y-axis is relative intensity
*in %). (c) Cryo-EM images of **[1]OAc-[2]OAc** in Opti-MEM complete medium (50 μM). (d)*
*High-resolution cryo-EM images of **[1]OAc** in Opti-MEM complete medium (50 μM); insert:*
average repeating distance as indicated by FFT (nm per repeating cycle).

4.2.4 Cytotoxicity and cell imaging of platinum(II) complexes. Considering the emissive
properties of the nanoaggregates of **[1]OAc** and **[2]OAc** in serum-containing aqueous solutions,
their biological properties in human cancer cell lines were further investigated. Both complexes

showed significant cytotoxicity in A549 lung cancer cell lines after 72 h incubation in the dark, with EC_{50} values of 10 µM for **[1]OAc** and 5 µM for **[2]OAc**, but negligible cytotoxicity in A431 human skin carcinoma, with EC_{50} values of 94 µM for **[1]OAc** and 68 µM for **[2]OAc** (Figure 4.4a). None of the complexes showed significant photocytotoxicity under blue light irradiation (455 nm, 5 minutes, 5.7 mW cm^{-2}, 1.7 J cm^{-2}) in normoxic condition (21% O_2, Figure 4.4a). This absence of light activation is in strong contrast with their palladium analogs, which showed strong photodynamic properties and negligible emission properties in similar conditions.[39] After 24 h treatment with 5 µM of **[1]OAc** and **[2]OAc,** a very high platinum cellular uptake observed, as measured with ICP-MS in A549 cells and A431 cells, up to 0.51±0.03 µg Pt/million cells (Figure 4.4b), which is more than 100-fold higher efficiency than that of cisplatin.[50] This result gives a strong indication that nanoaggregation can significantly improve metallodrug uptake. In contrast with the palladium analogues, A549 cells treated with 5.0 µM of the platinum complexes for 24 h and imaged by confocal microscopy showed strong deep-red luminescence in the 650-750 nm region under 638 nm excitation, which suggested that emissive nanoaggregates similar to those observed in cell-free conditions, are also formed inside the cancer cells (Figure 4.4c). Interestingly, continued confocal imaging for 48 h (Figure AIII.9) demonstrated that the emission of **[1]OAc** does not photobleach or degrade during that period, even upon cells splitting (Video S2), and thus that nanoaggregates formed via Pt…Pt interaction are not only surviving dioxygen and light, but also cell division.
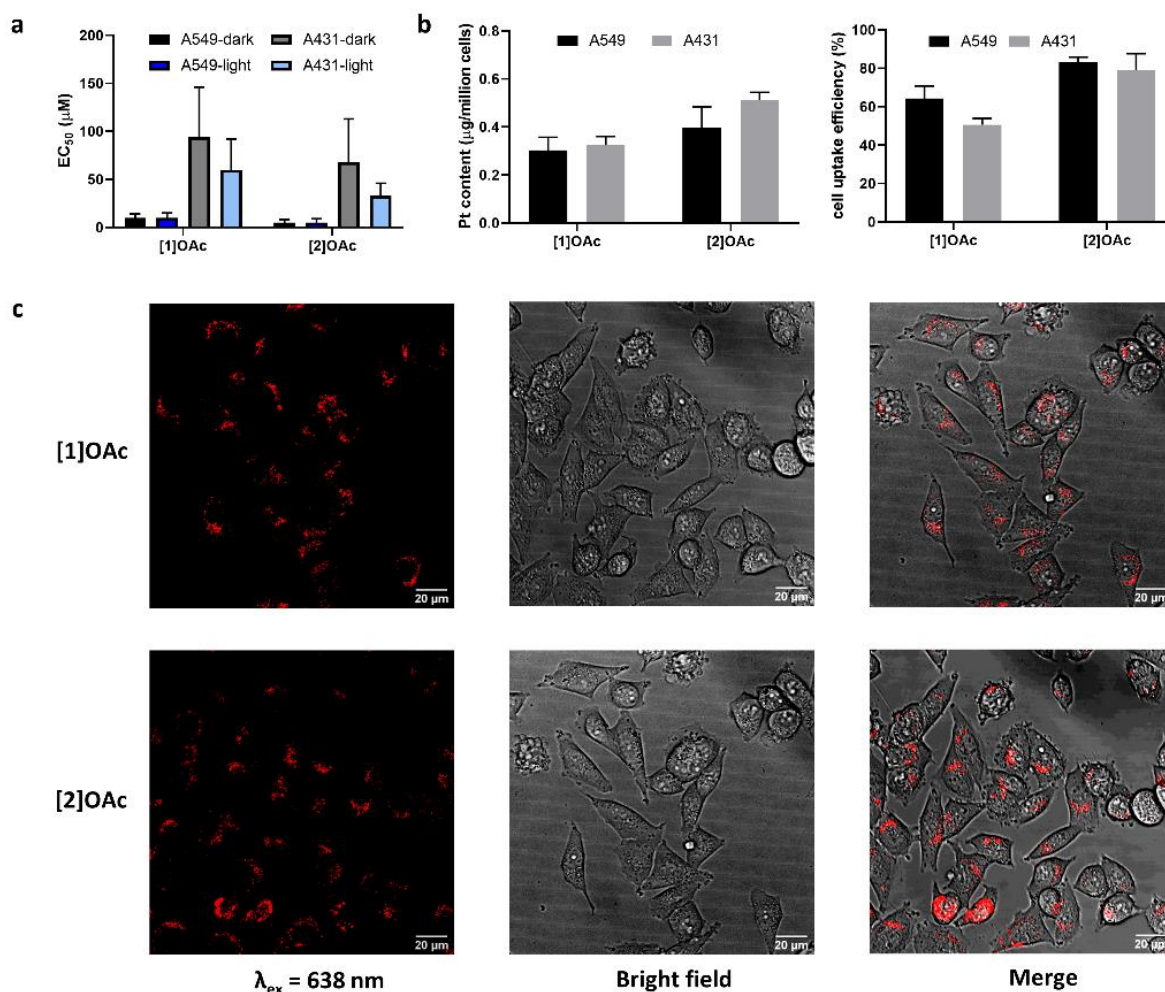
Figure 4.4 *(a) EC$_{50}$ values of **[1]OAc** or **[2]OAc** in the dark or under blue light irradiation (455 nm, 5 minutes, 5.7 mW cm^{-2}, 1.7 J cm^{-2}). (b) Pt content as measured by ICP-MS and cellular uptake efficiency (cellular Pt content/working solution Pt content $\times$100%) for A549 and A431 cells treated with **[1]OAc** and **[2]OAc** (concentration 5 μM). (c) Confocal images of A549 cells (scale bar 20 μm) after 24 h treatment with **[1]OAc** and **[2]OAc** (5 μM, λ_{ex} = 638 nm, λ_{em} = 650-750 nm).*

4.2.5 Cellular colocalization and uptake mechanism of platinum(II) complexes. Further colocalization imaging experiments were carried out at 552 nm excitation wavelength, where both complexes show a better absorbance compared with 638 nm. A549 cells were first treated with platinum complexes (5 µM) for 24 h, then co-stained for 15 min with Hoechst 33342 (0.1 µg/ml), a nucleus dye for living cells. The confocal images (Figure AIII.10) showed that **[1]OAc**-**[2]OAc** did not localize in the nucleus. More colocalization experiments were performed with green-emitting dyes for different organelles, such as lysosomes, mitochondria, Golgi apparatus, endoplasmic reticulum (ER), and lipid droplets. The overlapping images (Figure AIII.11-12) indicated an anti-correlation of **[1]OAc**-**[2]OAc** with the ER, lysosomes

and lipid droplets, suggesting they do not stay in such organelles after 24 h treatment. Though the emission of **[1]OAc** overlapped well with the Golgi apparatus (Pearson's correlation coefficient (PPC) values of 0.5-0.7, see Table AIII.2),[51] the emission characteristics of Golgi dye and metal complexes were significantly different: the former one showed a thread-like emissive pattern, while the platinum complex showed non-consecutive red dots in the cells. Thus it is elusive whether or not **[1]OAc** is present in the Golgi 24 h after treatment. For **[2]OAc**, the best co-localization pattern was obtained for the mitochondria, for which color-dependent pixel intensity curves (Figure 5a,b) and high PPC values (0.2-0.6, Table AIII.2) were obtained. Overall, 24 h after compound addition **[2]OAc** emitted primarily from the mitochondria, while the localization of **[1]OAc** in cells was unclear.

Because of their AIE deep red emission, the cell uptake mechanism of complexes could be monitored via flow cytometry. A549 cells were co-incubated with **[1]OAc** or **[2]OAc** (5 μM) and different cell uptake inhibitors, after which the variations of the relative fluorescent cell populations at 2 h were assessed by FACS.[52] The presence of self-assembled nanorods of the complexes in medium inspired us to particularly look into different inhibitors of endocytosis, an active transport mechanism for the uptake of nanoparticles across the cell membrane. Thus we chose a series of endocytosis and active transport inhibitors, including sodium azide (NaN₃, active transport inhibitor), pitstop 2 (clathrin-dependent endocytosis inhibitor), dynasore (dynamin-dependent endocytosis inhibitor), nocodazole (phagocytosis inhibitor), and wortmannin (macropinocytosis inhibitor).[53-55] As shown in Figure 5c, nocodazole and wortmannin did not result in inhibition of the relative deep-red fluorescent cell populations, thus excluding the role of phagocytosis and micropinocytosis in the drugs uptake. NaN₃ showed slight uptake inhibition for both complexes, suggesting that active transport and clathrin-dependent endocytosis are playing an active but limited role in compound uptake. The strongest response was obtained after treatment with dynasore and Pitstop 2, upon which the percentage of emissive cells was dramatically decreased, compared with the control groups only treated with the complexes. Specifically, pitstop 2 showed a more significant uptake inhibition for **[2]OAc** than **[1]OAc**, suggesting the different endocytic pathways for the isomeric compounds, while dynasore had an equal and large effect on both compounds. Overall, these data indicated that **[1]OAc** and **[2]OAc** enter into cells by dynamin-dependent and clathrin-dependent endocytosis, which is consistent with the hypothesis of uptake as nanoparticles.[56, 57]

Still, these flow cytometry experiments were based on the aggregation-induced deep red emission, and hence only measured internalization of the aggregated particles, but no detection

of the essentially non-emissive monomeric platinum complexes, which might be uptaken via energy-independent transport. Thus ICP-MS was used to detect the whole Pt content of A549 cells treated with the Pt complex alone at 37 °C (control), the complex alone at 4 °C, to check passive uptake, or the complex co-incubated with dynasore for 2 h. As showed in Figure 5d, dynasore inhibited the cellular uptake of the two Pt complexes, matching well with the flow cytometry analysis. At 4 °C, significant cellular uptake inhibition was observed for both complexes, resulting in 53% and 58% reduction of the Pt content for **[1]OAc** and **[2]OAc**, respectively (Table AIII.3), which accounts for the shutting of active uptake processes at low temperatures. On the other hand, there was still significant Pt uptake at low temperature, which means that not all Pt complexes are taken up by active processes. Overall, these results suggest that more than half of the platinum complexes are internalized in A549 cells by energy-dependent, endocytic transport, while a bit less than half of the metal complexes cross the cell membrane via passive diffusion or energy-independent channels.
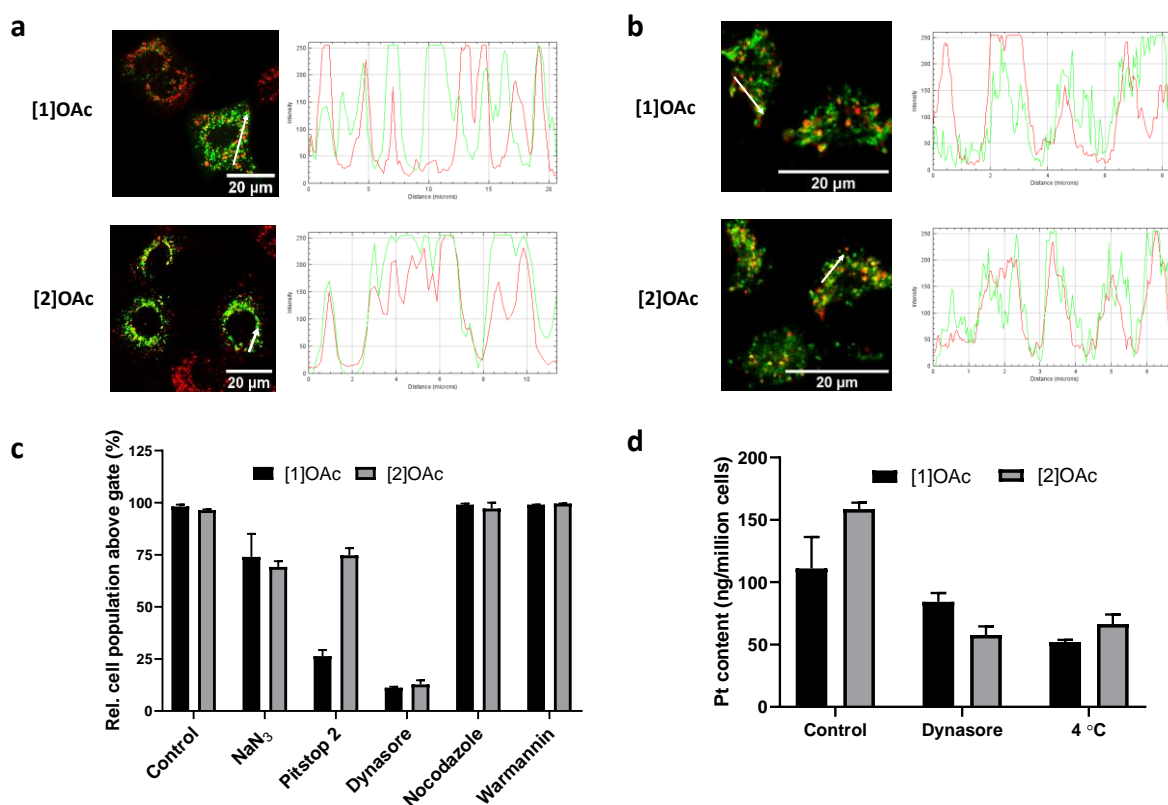

Figure 4.5 *Cellular uptake of **[1]OAc**-**[2]OAc** in A549 cells. (a)-(b) Overlapping images and pixel intensity curves of A549 cells treated with **[1]OAc** or **[2]OAc** (red color, 5 μM) and (a) Mitochondria Green Fluorescent Protein (GFP, green) or (b) MitoTracker Green FM (green color). (c) Relative fluorescent cell population (%), according to cell flow cytometry (FACS), after treatment of A549 cells with **[1]OAc**-**[2]OAc** (5 μM) and different cellular uptake*

*inhibitors. (d) Pt content, according to ICP-MS analysis, of A549 cells treated with **[1]OAc**-**[2]OAc** (5 μM) for 2 h at 37 °C, without (control) or with dynasore, or at 4 °C.*

4.2.6 Time evolution of [2]OAc inside A549 cells. As **[2]OAc** showed increased colocalization with mitochondria after 24 h, and its major internalization mechanism was endocytosis, we engaged into investigating the time evolution of its intracellular colocalization with lysosomes and mitochondria upon uptake. Following 3 h incubation with **[2]OAc** and fluorescent labeling of the lysosomes and mitochondria, fluorescent images of A549 cells were acquired at time points 3.5, 4.5, 5.0, 5.5, 6.0, 21.0 and 45.0 hours (time point zero was set to the time of addition of the compound). Volume-view images of representative cells at 3.5, 6.0, 21.0 and 45.0 hours are shown in Figure 6a. The top row shows the lysosomes (blue), the second row the mitochondria (green), the third row shows the **[2]OAc** compound (red), and the fourth and fifth row shows the merged fluorescence of **[2]OAc** (red) with lysosomes (blue) and mitochondria (green), respectively. Lysosomes fluorescence increased with incubation time, whereas mitochondria fluorescence exhibited a peak at 6.0 hours and a subsequent decrease, especially at the time point of 45.0 hours. **[2]OAc** fluorescence increased at time points 21.0 and 45.0 hours, with bigger aggregates clearly distinguishable inside the cells. An increase in the colocalization of **[2]OAc** with the mitochondria was observed with increasing time. This observation was confirmed quantitatively by plotting Mander's overlap coefficient vs. time (Figure 6b).[58] Colocalization of **[2]OAc** with the lysosomes (grey circles) was rather low (overlap coefficient below 0.15) for all time points, suggesting limited uptake of the nanoaggregated platinum compound by the lysosomes. However, these results conflict with the typical endocytosis mechanism that usually involves endosomes and lysosomes. This conflict may indicate that **[2]OAc** traffics to mitochondira directly after dynamin- and clathrin-mediumted endocytosis, an endocytotic mechanism that is unusual but was reported recently.[59] Alternatively, the accumulation of emissive nanoparticles in the mitochondria at 24 h could also be the result from passive uptake of the compound as monomer, migration to the mitochondria driven by the negative charge of the mitochondrial membrane ($[2]^+$ is monocationic), and re-assembly due to the increased local concentration of the monomer. The decrease in colocalization of **[2]OAc** with both the lysosomes and the mitochondria after 45.0 hours might be due either to partial degradation of the complex, or to disassembly; this is suggested also by Figure 6c, where the average deep-red fluorescent intensity of **[2]OAc** per cell shows a slight decrease at 45.0 hours, as compared to that at 21.0 hours. The mean **[2]OAc** intensity per cell exhibits an increase after 21.0 hours as compared to that for 3.5-6.0 hours, as shown in Figure

6c, probably due to the formation of larger aggregates. Although the increase is statistically significant, the difference is of the same order of magnitude in the intensity scale (a bit more than 6000 AU for 21.0 hours, vs approximately 5000 AU for 3.5-6.0 hours), whereas visually it appears more intense (Figure 6a, third row). This observation may be attributed to a non-linear relationship between the fluorescence intensity observed and the size of **[2]OAc** aggregates formed.[60] Altogether, these data confirmed the accumulation of deep-red emissive aggregates of **[2]OAc** inside the cellular environment already 3 h after treatment, the limited assistance of lysosomes during aggregates internalization, and a tendency of the compound to co-localize with the mitochondria.
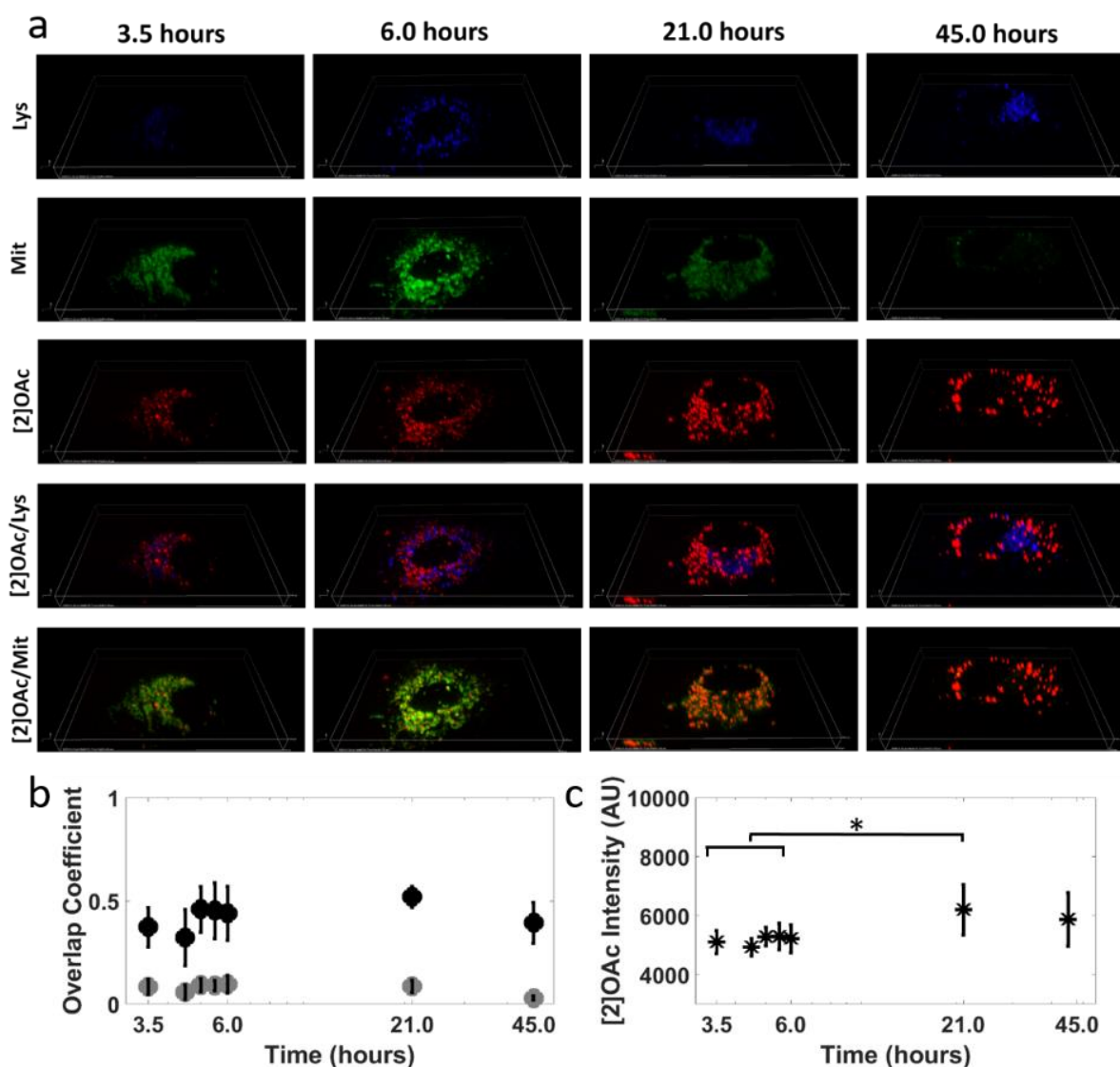

Figure 4.6 *(a) Fluorescent images of lysosomes (blue, top row), mitochondria (green, second row),* ***[2]OAc*** *(red) (third row), merged* ***[2]OAc*** *with lysosomes (fourth row) and merged* ***[2]OAc*** *with mitochondria (bottom row), at 3.5, 6.0, 21.0 and 45.0 hours after 3-hours incubation with* ***[2]OAc*** *(t=0-3 hours). (b) Quantification of* ***[2]OAc*** *colocalization with*

lysosomes (grey) or mitochondria (black) at 3.5, 4.5, 5.0, 5.5, 6.0, 21.0 and 45.0 hours after 3-hours incubation with **[2]OAc** *(t=0-3 hours). Overlap coefficients were calculated using Mander's Overlap Coefficient (MOC) with the Nikon Nis Elements Software and are shown as mean values ± standard deviations of an average of 8-16 cells per time point. (c)* **[2]OAc** *mean intensity per cell, at 3.5, 4.5, 5.0, 5.5, 6.0, 21.0 and 45.0 hours. Values are shown as means ± standard deviations of an average of 6-11 cells per time point. Statistical significance p-values were calculated using the Wilcoxon statistical test * p≤0.05.*

4.2.7 Determining the morphology of [2]OAc in the cell by cell-EM. The limited spatial resolution of confocal microscopy, and the conflicting observations of an endocytosis uptake with limited colocalization with the lysosomes, pushed us to use electron microscopy (EM) imaging to study the fate and morphology of the nanoparticles inside the cells. EM imaging of A549 cells incubated for 3 h, 5 h and 24 h with compound **[2]OAc** (5 µM) was performed. No nanoparticles were observed in the untreated cell control group (Figure AIII.13). On the other hand, many dark-contrasted spots were observed in the treated cells, indicative of nanoparticles of **[2]OAc** (Figure 7a-c). These nanoparticles were located in the mitochondria, which is in agreement with the confocal microscopy data. Note that the apparent morphology of nanoaggregates of **[2]OAc** in the mitochondria of sectioned cells looked like nanoparticles, which seemed different from the nanorod morphology observed in cell-free medium (Figure 4c). However, nanorods observed in absence of cells by cryo-EM, are not sectioned like in cell-EM, but lie flat in a plane that is essentially perpendicular to the electron beam, hence their length can be systematically imaged. It was hence difficult to distinguish, within the cell environment, the true morphology (*i.e.*, nanoparticles vs. nanorods) of the nanostructures made by **[2]OAc**. In addition, it was curious to notice that no nanoparticle was observed in the lysosomes or cytoplasm at any time point investigated by cell-EM. Combined with the observed endocytotic uptake mechanism found by FACS analysis and the low co-localization of lysosome-target dyes and aggregated **[2]OAc**, these results suggested that this compound performed a direct transfer from the dynamine- and clathrin-coated vesicles to the mitochondria, avoiding the classical endosome- and lysosome-assisted endocytosis process.[59] All in all, the cell-EM images at three different time points fit quite well the time-dependent confocal microscopy images, demonstrating the formation, following endocytosis, of nanostructures of **[2]OAc** in the mitochondria, without involvement of the endosome or lysosome, and without nanoparticle formation (or migration) in the cytoplasm.
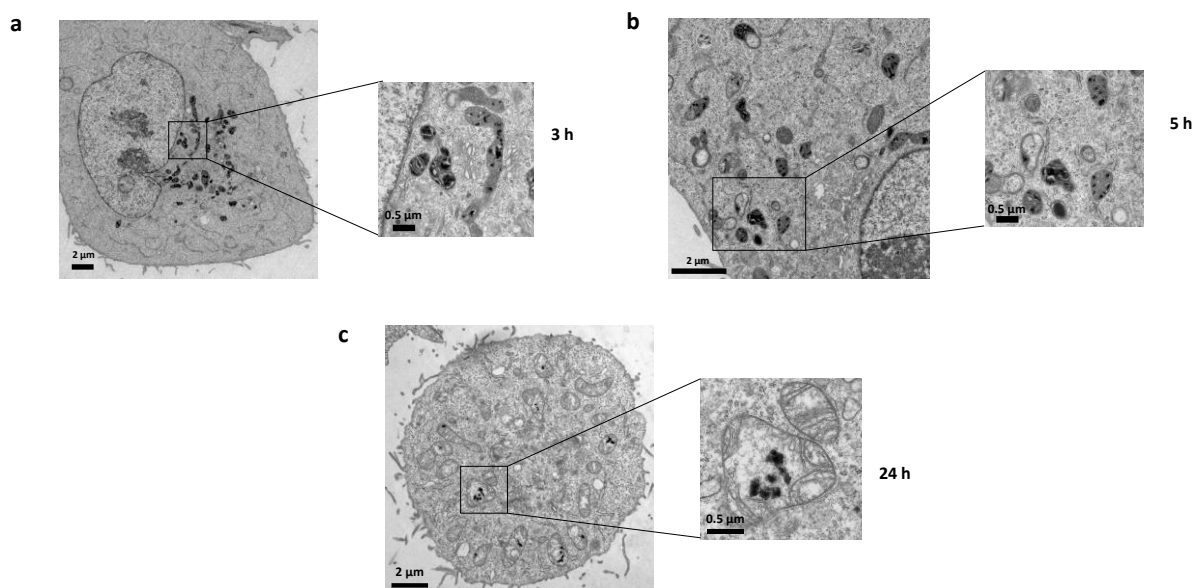
Figure 4.7 *EM images of A549 cells 24 h after treatment with **[2]OAc** (5 µM) at 3 h (a), 5 h (b) and 24 h (c) (scale bar 2 or 0.5 µm).*

4.3 Discussion

In recent years, the metallophilic interaction has developed as an essential form of supramolecular interaction, with many new applications, *i.e.* from OLED to bioimaging.[48, 61-64] Our group recently demonstrated that the palladium analog of **[1]OAc** could serve as a very efficient PDT agent that generated serum-stabilized, phototoxic but not-emissive, nanorods via Pd…Pd metallophilic interactions.[39] These nanorods are difficult to study in cells because they are non-emissive. By changing the metal center to platinum, we now demonstrate that similar self-assembly takes place with **[1]OAc** and **[2]OAc**. Remarkably, the metallophilic Pt…Pt interaction at the source of the nanorod self-assembly in the serum-containing medium now generates deep-red emission, which allows for studying the uptake and intracellular fate of these nanorods both by confocal microscopy and cellular EM.

The results of the uptake inhibition experiments suggested that dynamin- and (or) clathrin dependent endocytosis, a specific uptake pathway working via dynamin and clathrin proteins, are the main channels for the nanoparticles of **[1]OAc** and **[2]OAc** to cross the cell membranes. However, near half of the Pt complexes **[1]OAc** and **[2]OAc** were internalized into the cells via passive diffusion (or at least energy-independent channels), suggesting that the platinum complexes might exist both as aggregated nanoparticles and isolated molecules in the cell medium. Importantly, already after 3 h **[2]OAc** was found to locate in the mitochondria in an aggregated, emissive state. The confocal colocalization and cell-EM experiments excluded the

role of lysosomes in the cellular movement of **[2]OAc**. These apparently conflicting results can be explained by a recent report that exogenous molecules may also traffic to mitochondria directly from the plasma membrane by clathrin-mediumted endocytosis, and entry of the endosome into mitochondria using microtubule-dependent active transport.[59]

Overall, two (co-existing) mechanisms can be proposed to interpret the cellular uptake and time-dependent localization of **[2]OAc**. First, an energy-dependent mechanism can be proposed (Scheme 1): small nanoaggregates enter into cells *via* endocytosis, and traffic to the mitochondria directly via the clathrin- or dynamine-coated endosomes. These aggregates are small enough not to be detected by EM, but big enough to contribute to the phosphorescence signal detected by FACS. As a side note, this process is very fast and efficient, as it takes place within 3 h and leads to above half of the cellular uptake of the compound. The second mechanism involves passive uptake of **[2]OAc** as isolated molecules. These isolated molecules are invisible by cell EM and not emissive, but due to their positive charge they diffuse to the negatively charged mitochondrial membrane, where re-assembly occurs, contributing to the accumulation of larger and emissive nanoparticles in the mitochondria.
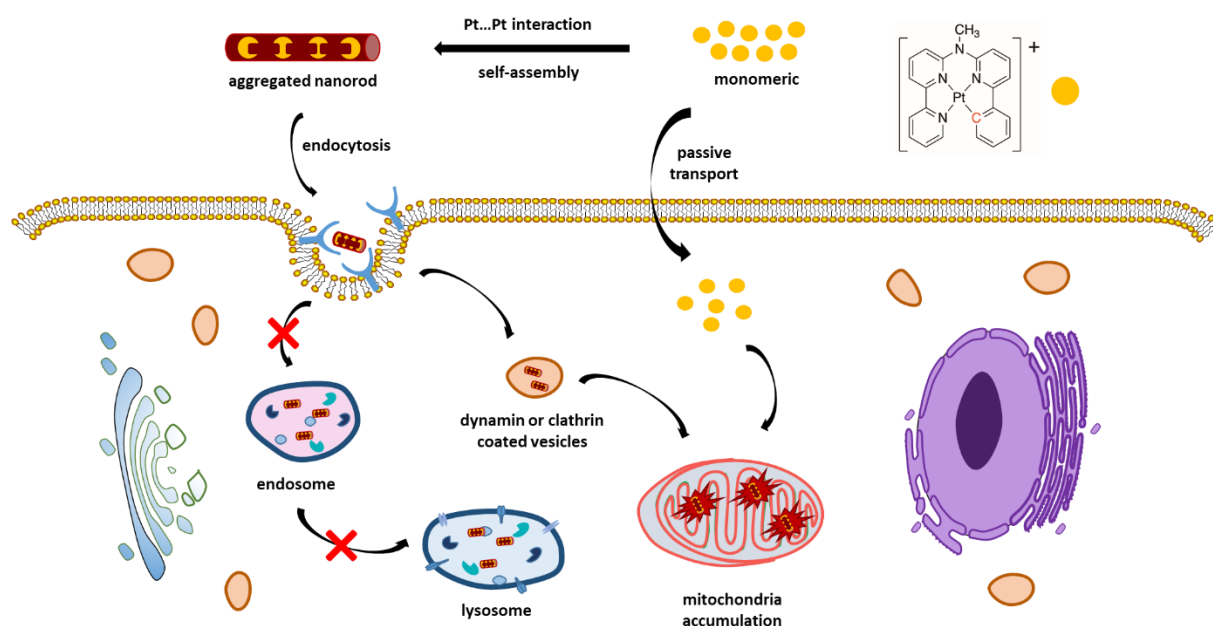
Scheme 1. *Schematically cellular uptake and movement of [2]OAc.*

Whatever the mechanism for cellular uptake, Pt nanoparticles were observed in the mitochondria, suggesting that the Pt…Pt interaction is a reliable supramolecular interaction for building theranostic platforms in cells, because it survives cell metabolism and even cell division. This interaction could be used for making supramolecular sensors or devices that can penetrate inside a cell by endocytosis, rearrange, and relocate to perform a specific function

(here mitochondria staining). Importantly, these self-assembled sensors work at high wavelengths that are ideal for bioimaging. In the cell medium, these nanoaggregates are stabilized by plasma proteins, which generates nanorods, while in mitochondria they might have different, particle-like morphologies. Altogether, proteins, as well as salts, appear to play a critical role in balancing the repulsive (electrostatics) and attractive (π-π stacking, d_z^2 overlap) forces at the origin of the metallophilic interaction. The different proteins present in the cell medium, lysosome, cytosol, and mitochondria, may lead to different forms of self-assembly, which contributes to the dynamics of the complex inside the cell.

4.4 Conclusion

In summary, this work demonstrated that two cyclometalated platinum complexes generated self-assembled, protein-stabilized nanorods in cell medium via Pt…Pt interaction. Due to their supramolecular aggregation properties, these compounds cross the cell membrane *via* a combination of passive uptake (for the monomers) and dynamin- and clathrin-dependent endocytosis (for the nanoparticles). The nanoparticles directly move to mitochondria *via* the spefic dynamin- and clathrin-coated vesicles, and re-assemble inside the mitochondria as deep-red phosphorescent nanoparticles. These nanoparticles survive both in living and dividing cells, while showing very limited phototoxicity. Overall, this set of platinum complexes demonstrate new perspectives for using the metallophilic interaction to build supramolecular nanosystem that, at high concentration, can kill cancer cells, but at low concentration, may be used as deep-red trackers for different organelles – here the mitochondria.

4.5 Experimental section

4.5.1 Compounds preparations. The ligands **HMeL^1** and **HMeL^2** were prepared as described in chapter 3. The platinum complexes **[1]OAc** and **[2]OAc** were synthesized using the methods described in chapter 3, using platinum(II) bis(acetylacetonate) instead of palladium(II) acetate.
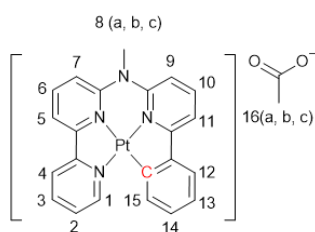
[1]OAc
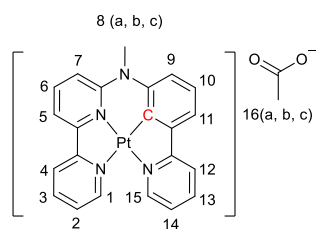
A mixture of the ligand **HMeL^1** (68 mg, 0.2 mmol), Pt(acac)$_2$ (79 mg, 0.2 mmol) and tetrabutylammonium acetate (10 mg, 0.04 mmol) was dissolved in CH$_3$COOH (50 mL) and heated at 135 °C under an N$_2$ atmosphere for 6 days. The solvent was rotary evaporated to obtain a yellow solid, which was washed with EtOAc (100 mL) and diethyl ether (50 mL), and dried under vacuum, to finally obtain **[1]OAc** as analytically pure product (Yield: 38 mg, 0.06 mmol, 32%). **HRMS** (cation): m/z calcd 532.1101 [C$_{22}$H$_{17}$N$_4$Pt]$^+$, obsd 532.1097. **^{1}H NMR** (400 MHz,

Methanol-d_4) 9.03 (1 H, s, H[1]), 8.79 (1 H, d, J 5.6, H[15]), 8.55 (1 H, d, J 8.2, H[4]), 8.32 (1 H, t, J 7.8, H[3]), 8.19 (1 H, t, J 8.1, H[6]), 8.11 (1 H, t, J 7.7, H[13]), 8.04 (2 H, t, J 6.8, H[5], H[12]), 7.88 (1 H, s, H[2]), 7.63 (1 H, d, J 8.7, H[7]), 7.54 (1 H, d, J 7.4, H[11]), 7.48 (1 H, d, J 7.1, H[14]), 7.37 (1 H, t, J 7.6, H[10]), 7.30 (1 H, d, J 8.0, H[9]), 3.88 (3 H, d, J 1.6, H[8]), 1.90 (3 H, d, J 1.5, H[16]). **^{13}C APT-NMR** (101 MHz, MeOD) δ 154.4, 150.0, 148.5, 145.8, 141.3, 140.7, 139.2, 138.4, 128.9, 127.7, 126.6, 124.8, 124.5, 121.4, 120.5, 119.2, 118.8, 116.6, 42.4. Elemental analysis calcd for **[1]OAc** + 2H$_2$O: C, 45.93; H, 3.85; N, 8.93; Found for **[1]OAc** + 2H$_2$O: C, 46.07; H, 3.97; N, 8.88.

[2]OAc

[2]OAc was synthesized using the same method as for **[PtMeL^1]OAc**, but starting from ligand **HMeL^2** (34 mg, 0.1 mmol). The yield in **[2]OAc** was 93% (55 mg, 0.093 mmol). **HRMS** (cation): m/z calcd 532.1101 [C$_{22}$H$_{17}$N$_4$Pt]$^+$, obsd 532.1093. **^{1}H NMR** (400 MHz, Methanol-d_4) 8.79 (1 H, d, J 5.6, H[1]), 8.18 (2 H, d, J 4.3, H[3], H[4]), 8.10 (1 H, t, J 8.1, H[6]), 7.87 (1 H, t, J 8.1, H[10]), 7.80 (1 H, d, J 7.7, H[5]), 7.55 (1 H, q, J 4.9, H[2]), 7.50 (1 H, d, J 8.6, H[7]), 7.46 – 7.41 (5 H, m, H[12]), 7.37 (1 H, d, J 7.7, H[11]), 7.13 – 7.09 (2 H, m, H[13], H[14]), 7.07 (1 H, d, J 8.5, H[9]), 7.01 (1 H, d, J 7.3, H[15]), 3.52 (3 H, s, H[8]), 1.92 (3 H, s, H[16]). **^{13}C APT-NMR** (101 MHz, Methanol-d_4) δ 157.0, 150.6, 149.7, 149.1, 148.0, 145.5, 143.9, 139.8, 139.3, 139.2, 130.8, 129.1, 126.9, 124.8, 124.2, 123.9, 117.5, 117.3, 113.2, 113.0, 42.7. Elemental analysis calcd for **[2]OAc** + 1.5H$_2$O: C, 46.60; H, 3.75; N, 9.06; Found for **[2]OAc** + 1.5H$_2$O: 46.37, 3.79, 9.01. The CH$_3$COO$^-$ counter ion of **[2]$^+$** was changed to **PF$_6^-$** ion by adding excess KPF$_6$ to a water solution of the metal acetate complex, to obtain a precipitate of **[2]PF$_6$** that was collected by filtration and dried. Single crystals of **[2]PF$_6$** were obtained through vapor diffusion of diethyl ether into a MeOH/DCM solution of **[2]PF$_6$**. The single X-ray crystallography of **[2]PF$_6$** was determined via methods described in section 3.5.3. CCDC number of **[2]PF$_6$** is 2001190.

4.5.2. DFT calculation. The geometries of the monomeric and dimeric complexes were optimized in water solvent with the Amsterdam Density Functional (ADF) software package at the density functional theory (DFT) level employing the PBE0 hybrid density functional[63] and the TZP (triple-ζ polarized) Slater-type basis set. The time-dependent DFT (TD-DFT) calculations were then performed at the same level to evaluate the optical properties. The vertical excitation energy was efficiently calculated by the corresponding TD-DFT method. The first 20 excited singlet states were taken into account in the calculations of the absorption

spectra. Solvent effects were included using the continuum solvation model (COSMO) in all calculations to describe the water environment.

4.5.3 TEM measurement of metal complexes in Opti-MEM complete medium. The TEM experiments were carried via TEM JEOL 1010:100 kV transmission electron microscope using Formvar/Carbon coated copper grid from Polysciences Inc. For the preparation of samples, each drop (15 µL) of complex solutions (50 µM) was deposited on parafilm. The grids were placed on top of the drops for 2 min, then the excess liquid on the grid was removed by filter paper, and the grid was dried for 2 h before the TEM measurement. The TEM measurements were carried out in vacuum conditions.

4.5.4 Cryo-EM measurement. 6 µL of sample ([complex] = 50 µM) was applied to a freshly glow-discharged carbon 200 mesh Cu grid (Lacey carbon film, Electron Microscopy Sciences, Aurion, Wageningen, The Netherlands). Grids were blotted for 3 s at 99% humidity in a Vitrobot plunge-freezer (FEI VitrobotTM Mark III, Thermo Fisher Scientific). Cryo-EM images were collected on a Titan/Krios operating at 300 kV or on a Talos L120C operating at 120 kV (NeCEN, Leiden University). In the case of Titan/Krios, images of **[1]OAc** were recorded manually at a nominal magnification of 3600x, 33000x or 81000x yielding a pixel size at the specimen of 31.8Å, 3.5Å or 1.4Å , respectively. In the case of Talos L120C, images of **[2]OAc** were recorded manually at a nominal magnification of 13500x yielding a pixel size at the specimen of 2.3 Å.

4.5.5 Cell culture and photocytotoxicity experiments. The process for cell culture and photocytotoxicty experiments are described in section 2.4.6 of chapter 2.

4.5.6 Cellular uptake experiments. A549 and A431 cells were seeded in a 12-well plate (2×10^5 cells, 1 mL Opti-MEM complete per well). At t = 24 h, the cells were treated with complexes **[1]OAc** or **[2]OAc** (5 µM, 0.5 mL Opti-MEM complete). After 24 h treatment, the cells were harvested by trypsin (5% v/v in PBS), counted via trypan blue, and centrifuged in 15 mL tubes. After removing the supernatant, the cell pellets were lysed by adding 0.5 mL HNO_3 (65%) into the tubes, keeping for 10 min and sonicating for 30 min at room temperature. After that, the cell solution was diluted to 10 mL using milli-Q water, and the Pt content in the solution was determined using ICP-MS (NexION 2000, PerkinElmer). Each experiment was carried out for 3 times.

4.5.7 Confocal experiments in A549 cells. The cell-imaging experiments were carried out using confocal microscopy. In brief, 200 µL aliquots containing 2×10^4 A549 cells were first

seeded onto a μ-slide 8-well confocal plate (ibidi). At t = 24 h, the wells were treated with **[1]OAc** or **[2]OAc** (5 μM). At t = 47.5 h, the wells were treated with a chemical dye, unless otherwise stated. A 20X oil immersion objective was used for all imaging, with an additional zoom factor from 1.0X – 3.0X. Control wells were used to set laser and gain intensity such that background signal was eliminated or negligible prior to measurement of target wells. For nucleus staining, A549 cells were treated with Hoechst 33342 (0.1 μg/mL) for 15 min. For GFP experiments, CellLight™ GFP expression vector solutions were added to wells at t = 24 h with the drug compounds under study for a full 24-h incubation before measurement, as directed by the included manufacturer protocol. For MitoTracker™ Green FM (ThermoFisher), a 1 mM stock solution was prepared from dry product, which was diluted in Opti-MEM complete to the desired concentration (100 nM) for treatment and incubation 30 min before measurement. For HCS LipidTOX™ Green neutral lipid stain, LysoTracker™ Green DND-26 and BODIPY™ FL C5-Ceramide complexed to BSA golgi dye (ThermoFisher), the provided stock solutions were similarly diluted and treated according to the manufacturer's protocol. All image analyses were processed using ImageJ. Colocalization measurements were taken using the ImageJ plugin Coloc2 with PSF = 5.0 and verified with Costes' significance test. Linear correlation graphs were created using the RGB Profile Plot plugin.

4.5.8 [1]OAc real-time uptake. Uptake of **[1]OAc** was captured via live cell imaging, with fluorescence Spinning Disk Confocal Microscopy. 2×10^4 A549 cells were seeded in a μ-slide 8-well confocal plate (ibidi) and allowed to adhere for 24 hours. Cells had been treated with **[1]OAc** (5 μM) for 15 minutes when image acquisition started. Fluorescence and bright-field images were acquired at 50 seconds interval for 12 hours. Control wells were used to set laser and gain intensity such as to eliminate the background and exclude signal saturation.

4.5.9 Time-dependent colocalization of [2]OAc with lysosomes and mitochondria. To investigate the colocalization over time of **[2]OAc** with the lysosomes and the mitochondria, 7×10^4 A549 cells were seeded in a round dish (ibidi) and allowed to adhere for 24 hours, then treated with **[2]OAc** (5 μM) for 3 hours after which time the compound was removed. Fluorescence Spinning Disk Confocal 3D images were captured at time points 3.5, 4.5, 5.0, 5.5, 6.0, 21.0 and 45.0 hours after addition of the compound (time=0), for 8-16 cells per time point. At each time point, 3D fluorescent and bright-field images were captured with a step size of 200 nm. Image processing and extraction of the Mander's Overlap Coefficient (MOC) was carried out for each focal plane using the NIS Elements software (Nikon Corporation, Japan). Further data processing was performed with Matlab. Quantification of **[2]OAc** intensity inside

the cells over time was performed by averaging the mean **[2]OAc** fluorescence intensity per cell, for 6-11 cells per time point.

4.5.10 Cell uptake inhibition experiment using flow cytometry. At t = 0 h, 2.0×10^5 A549 cells (1 mL, Opti-MEM complete) were seeded into flat bottom 24-well plates (Cellstar® F-bottom No.622160). At t = 21 h, all wells except controls were treated with inhibitor solutions prepared in Opti-MEM complete unless otherwise noted at the following treatment concentrations: NaN_3 (1 mg / mL), Pitstop 2 (20 µM, Opti-MEM without fetal calf serum or other additives), Dynasore (80 µM), Nocodazole (40 µM), and Wortmannin (250 nM). At t = 22 h, stock solutions of drug compounds were added to each well to a final concentration of 5 µM. At t = 24 h, all wells were prepared and measured by flow cytometry, with the parameter "RED-B" (488 nm excitation, 661±15 nm emission) for each drug compound. The experiments were carried out in three independent experiments and analyzed via FlowJ 10.

4.5.11 EM imaging in A549 cells. A549 cells (3×10^5 cells/mL, 9 mL, Opti-MEM complete medium) were seeding into 10 cm diameter plate and incubated for 24 h under normoxic condition (21% O_2, 5% CO_2, 37 ˚C). After that, the cells were treated with **[2]OAc** (5 µM) for another 24 h under normoxic condition. Then cells were fixed for 2 h in 1.5% glutaraldehyde in 0.1M Cacodylate buffer at room temperature and post-fixed first for 1 h in 1% Osmium tetroxide and then for 1 h in 1% Uranyl acetate. The fixed cells were dehydrated through a series of ethanol and flat embedded in Epon. Ultrathin sections (50 nm) of the embedded cells were produced in a Leica UC6 ultra-microtome and transferred to a formvar and cabon coated copper grid. The sections were stained with 7% Uranyl acetate and 1% Lead citrate before imaging in the TEM. Electron microscopy images were recorded using a Tecnai 12 TEM (FEI Company) equipped with an EAGLE 4×4 K digital camera using a magnification of 13,000x.

4.6 Acknowledgments

4.7 References

1. V. W. Yam, V. K. Au and S. Y. Leung, *Chem. Rev.*, 2015, **115**, 7589-7728.

2. A. Diez, J. Fornies, C. Larraz, E. Lalinde, J. A. Lopez, A. Martin, M. T. Moreno and V. Sicilia, *Inorg. Chem.*, 2010, **49**, 3239-3251.

3. Y. S. Wong, M. C. Tang, M. Ng and V. W. Yam, *J. Am. Chem. Soc.*, 2020, **142**, 7638-7646.

4. M. A. Soto, V. Carta, R. J. Andrews, M. T. Chaudhry and M. J. MacLachlan, *Angew. Chem. Int. Ed.*, 2020, **59**, 10348-10352.

5. W. Lu, Y. Chen, V. A. Roy, S. S. Chui and C. M. Che, *Angew. Chem. Int. Ed.*, 2009, **48**, 7621-7625.

6. A. Aliprandi, D. Genovese, M. Mauro and L. De Cola, *Chem. Lett.*, 2015, **44**, 1152-1169.

7. J. Romanova, M. R. Ranga Prabhath and P. D. Jarowski, *J. Phys. Chem.*, 2016, **120**, 2002-2012.

8. M. Y. Yuen, V. A. Roy, W. Lu, S. C. Kui, G. S. Tong, M. H. So, S. S. Chui, M. Muccini, J. Q. Ning, S. J. Xu and C. M. Che, *Angew. Chem. Int. Ed.*, 2008, **47**, 9895-9899.

9. X. Yan, T. R. Cook, P. Wang, F. Huang and P. J. Stang, *Nat. Chem.*, 2015, **7**, 342-348.

10. H. L. Au-Yeung, S. Y. Leung, A. Y. Tam and V. W. Yam, *J. Am. Chem. Soc.*, 2014, **136**, 17910-17913.

11. K. Li, G. S. Ming Tong, Q. Wan, G. Cheng, W. Y. Tong, W. H. Ang, W. L. Kwong and C. M. Che, *Chem. Sci.*, 2016, **7**, 1653-1673.

12. A. Aliprandi, M. Mauro and L. De Cola, *Nat. Chem.*, 2016, **8**, 10-15.

13. H. Xiang, J. Cheng, X. Ma, X. Zhou and J. J. Chruma, *Chem. Soc. Rev.*, 2013, **42**, 6128-6185.

14. M. Mauro, A. Aliprandi, D. Septiadi, N. S. Kehr and L. De Cola, *Chem. Soc. Rev.*, 2014, **43**, 4144-4166.

15. N. A. Smith and P. J. Sadler, *Philos. Trans. R. Soc. A*, 2013, **371**, 20120519.

16. C. Ash, M. Dubec, K. Donne and T. Bashford, *Lasers in Med. Sci.*, 2017, **32**, 1909-1918.

17. D. Septiadi, A. Aliprandi, M. Mauro and L. De Cola, *RSC Adv.*, 2014, **4**, 25709-25718.

18. J. L. Tsai, T. Zou, J. Liu, T. Chen, A. O. Chan, C. Yang, C. N. Lok and C. M. Che, *Chem. Sci.*, 2015, **6**, 3823-3830.

19. C.-K. Koo, B. Lam, S.-K. Leung, M. H.-W. Lam and W.-Y. Wong, *J. Am. Chem. Soc.*, 2006, **128**, 16434-16435.

20. C. Y.-S. Chung, S. P.-Y. Li, M.-W. Louie, K. K.-W. Lo and V. W.-W. Yam, *Chem. Sci.*, 2013, **4**, 2453-2462.

21. L. Y. Liu, H. Fang, Q. Chen, M. H. Chan, M. Ng, K. W. Wang, W. Liu, Z. Tian, J. Diao, Z. W. Mao and V. W. W. Yam, *Angew. Chem. Int. Ed.*, 2020, DOI: 10.1002/anie.202007878.

22. N. Metzler-Nolte and Z. Guo, *Dalton Trans.*, 2016, **45**, 12965-12965.

23. X. Wang, X. Wang, S. Jin, N. Muhammad and Z. Guo, *Chem. Rev.*, 2019, **119**, 1138-1192.

24. N. Cutillas, G. S. Yellol, C. de Haro, C. Vicente, V. Rodríguez and J. Ruiz, *Coord. Chem. Rev.*, 2013, **257**, 2784-2797.

25. S. C. Kui, F. F. Hung, S. L. Lai, M. Y. Yuen, C. C. Kwok, K. H. Low, S. S. Chui and C. M. Che, *Chem. Eur. J.*, 2012, **18**, 96-109.

26. L. J. Chen and H. B. Yang, *Acc. Chem. Res.*, 2018, **51**, 2699-2710.

27. M. L. Saha, X. Yan and P. J. Stang, *Acc. Chem. Res.*, 2016, **49**, 2527-2539.

28. C. N. Lok, T. Zou, J. J. Zhang, I. W. Lin and C. M. Che, *Adv. Mater.*, 2014, **26**, 5550-5557.

29. W. Zhang, M. Wang, W. Tang, R. Wen, S. Zhou, C. Lee, H. Wang, W. Jiang, I. M. Delahunty, Z. Zhen, H. Chen, M. Chapman, Z. Wu, E. W. Howerth, H. Cai, Z. Li and J. Xie, *Adv. Mater.*, 2018, **30**, e1805557.

30. L. Cheng, C. Wang, L. Feng, K. Yang and Z. Liu, *Chem. Rev.*, 2014, **114**, 10869-10939.

31. B. Yang, Y. Chen and J. Shi, *Chem*, 2018, **4**, 1284-1313.

32. H. Kang, S. Hu, M. H. Cho, S. H. Hong, Y. Choi and H. S. Choi, *Nano Today*, 2018, **23**, 59-72.

33. D. M. Samhadaneh, G. A. Mandl, Z. Han, M. Mahjoob, S. C. Weber, M. Tuznik, D. A. Rudko, J. A. Capobianco and U. Stochaj, *ACS Appl. Bio Mater.*, 2020, **3**, 4358-4369.

34. Y. Feng, H. Chen, Y. Wu, I. Que, F. Tamburini, F. Baldazzi, Y. Chang and H. Zhang, *Biomaterials*, 2020, **230**, 119637.

35. M. Buchner, P. Garcia Calavia, V. Muhr, A. Kroninger, A. J. Baeumner, T. Hirsch, D. A. Russell and M. J. Marin,

Photochem. Photobiol. Sci., 2019, **18**, 98-109.

36.   J. Zhao and M. H. Stenzel, *Polym. Chem.*, 2018, **9**, 259-272.

37.   J. Chen, J. Li, J. Zhou, Z. Lin, F. Cavalieri, E. Czuba-Wojnilowicz, Y. Hu, A. Glab, Y. Ju, J. J. Richardson and F. Caruso, *ACS Nano*, 2019, **13**, 11653-11664.

38.   S. Behzadi, V. Serpooshan, W. Tao, M. A. Hamaly, M. Y. Alkawareek, E. C. Dreaden, D. Brown, A. M. Alkilany, O. C. Farokhzad and M. Mahmoudi, *Chem. Soc. Rev.*, 2017, **46**, 4218-4244.

39.   X. Q. Zhou, M. Xiao, V. Ramu, J. Hilgendorf, X. Li, P. Papadopoulou, M. A. Siegler, A. Kros, W. Sun and S. Bonnet, *J. Am. Chem. Soc.*, 2020, **142**, 10383-10399.

40.   X. Q. Zhou, A. Busemann, M. S. Meijer, M. A. Siegler and S. Bonnet, *Chem. Commun.*, 2019, **55**, 4695-4698.

41.   L. Zong, Y. Xie, C. Wang, J. R. Li, Q. Li and Z. Li, *Chem. Commun.*, 2016, **52**, 11496-11499.

42.   M. Yamaguchi, S. Ito, A. Hirose, K. Tanaka and Y. Chujo, *Mater. Chem. Front.*, 2017, **1**, 1573-1579.

43.   J. Mei, N. L. Leung, R. T. Kwok, J. W. Lam and B. Z. Tang, *Chem. Rev.*, 2015, **115**, 11718-11940.

44.   H. Qian, M. E. Cousins, E. H. Horak, A. Wakefield, M. D. Liptak and I. Aprahamian, *Nat. Chem.*, 2017, **9**, 83-87.

45.   L. Ravotto and P. Ceroni, *Coord. Chem. Rev.*, 2017, **346**, 62-76.

46.   Y. Ai, Y. Li, H. L. Fu, A. K. Chan and V. W. Yam, *Chem. Eur. J.*, 2019, **25**, 5251-5258.

47.   J. Zhao, Z. Feng, D. Zhong, X. Yang, Y. Wu, G. Zhou and Z. Wu, *Chem. Mater.*, 2018, **30**, 929-946.

48.   Z. Gao, Y. Han, Z. Gao and F. Wang, *Acc. Chem. Res.*, 2018, **51**, 2719-2729.

49.   Y. Zhu, M. Zhang, L. Luo, M. R. Gill, C. De Pace, G. Battaglia, Q. Zhang, H. Zhou, J. Wu, Y. Tian and X. Tian, *Theranostics*, 2019, **9**, 2158-2166.

50.   V. H. S. van Rixel, A. Busemann, M. F. Wissingh, S. L. Hopkins, B. Siewert, C. van de Griend, M. A. Siegler, T. Marzo, F. Papi, M. Ferraroni, P. Gratteri, C. Bazzicalupi, L. Messori and S. Bonnet, *Angew. Chem. Int. Ed.*, 2019, **58**, 9378-9382.

51.   K. W. Dunn, M. M. Kamocka and J. H. McDonald, *Am. J. Physiol. Cell Physiol.*, 2011, **300**, C723-742.

52.   C. A. Puckett, R. J. Ernst and J. K. Barton, *Dalton Trans.*, 2010, **39**, 1159-1170.

53.   J. Yang, J. Tu, G. E. M. Lamers, R. C. L. Olsthoorn and A. Kros, *Adv. Healthc. Mater.*, 2017, **6**, 1700759.

54.   D. Dutta, C. D. Williamson, N. B. Cole and J. G. Donaldson, *PLOS One*, 2012, **7**, e45799.

55.   G. Preta, J. G. Cronin and I. M. Sheldon, *Cell Commun. Signal.*, 2015, **13**, 24.

56.   O. Harush-Frenkel, N. Debotton, S. Benita and Y. Altschuler, *Biochem. Biophys. Res. Commun.*, 2007, **353**, 26-32.

57.   T.-G. Iversen, T. Skotland and K. Sandvig, *Nano Today*, 2011, **6**, 176-185.

58.   E. M. M. Manders, F. J. Verbeek and J. A. Aten, *J. Microsc.*, 1993, **169**, 375-382.

59.   Z. Wei, W. Su, H. Lou, S. Duan and G. Chen, *J. Mol. Cell. Biol.*, 2018, **10**, 539-548.

60.   Z. Zolmajd-Haghighi and Q. S. Hanley, *Biophys. J.*, 2014, **106**, 1457-1466.

61.   Z. Gao, P. A. Korevaar, R. Zhong, Z. Wu and F. Wang, *Chem. Commun.*, 2018, **54**, 9857-9860.

62.   L. Barrientos, S. Miranda-Rojas and F. Mendizabal, *Int. J. Quantum Chem.*, 2018, **119**, e25675.

63.   Q. Wan, W.-P. To, X. Chang and C.-M. Che, *Chem*, 2020, **6**, 945-967.

64.   X. Yin, S. A. Warren, Y. T. Pan, K. C. Tsao, D. L. Gray, J. Bertke and H. Yang, *Angew. Chem. Int. Ed.*, 2014, **53**, 14087-14091.